Interaction of C_{60} with Carbon Nanotubes and Graphite

Hendrik Ulbricht, Gunnar Moos, and Tobias Hertel

Fritz-Haber-Institut der Max-Planck-Gesellschaft, Faradayweg 4-6, 14195 Berlin, Germany

The interaction of C_{60} with single-wall carbon nanotubes (SWNTs) and graphite is studied experimentally by thermal desorption spectroscopy and theoretically by molecular-mechanics and molecular-dynamics calculations. The van der Waals parameters and force field for C_{60}-graphene and C_{60}-SWNT interactions are derived from the low-coverage C_{60} binding energy to the graphite surface. We use these to compare the efficiency of different mechanisms by which C_{60} can be encapsulated into SWNTs.

Carbon nanotubes (CNTs) have unique potential as multifunctional materials in nanoscaled gas sensors [1], molecular field effect transistors [2,3], as additives for composite materials [4], and more. Their synthesis and functionalization, aiming at the fabrication of materials with tailored properties, present an important challenge in the exploitation of their potential for future technologies. Our understanding of the microscopic mechanisms and forces underlying the formation of functionalized CNTs and CNT-hybrid structures is an important prerequisite for the successful optimization of such fabrication processes.

The combination of one-dimensional single-wall carbon nanotubes (SWNTs) with zero-dimensional fullerenes by encapsulation of C_{60} into the nanotubes [5,6] yields so-called "peapods"—a material with unique electronic structure [7] whose properties are currently studied with great effort. In particular, the mechanism of C_{60} encapsulation is still discussed controversially [8]. The interaction of C_{60} with the graphitic surface of SWNTs is expected to be predominantly through dispersion forces which are also important for the cohesive energy of graphite and C_{60} crystals [9,10]. However, dispersion forces are notoriously difficult to determine theoretically, and it was noted early on that experimental data are needed as a benchmark for further theoretical investigations [11]. Here, we report on the first experimental determination of van der Waals (VDW) parameters describing C_{60}-graphene and C_{60}-CNT interactions. Previous VDW potentials for C_{60}-SWNT interactions were based on the combination of C_{60}-C_{60} VDW parameters with those obtained for graphene-graphene interactions using the empirical combining rules for VDW potentials [12,13]. The scarce experimental data on the strength of VDW interactions in graphitic systems in general and its complete nonexistence for the C_{60}-graphene interaction, in particular, stimulated this investigation in an attempt to determine VDW parameters which permit one to explore the energetics and dynamics of C_{60}-SWNT interactions in further detail. To this end, we studied the interaction

of C_{60} with highly oriented pyrolytic graphite (HOPG) and SWNT bundles using thermal desorption spectroscopy. Empirical VDW constants are derived from the C_{60}-graphite binding energy. This allows one to calculate C_{60}-SWNT potential energy surfaces (PESs) and identify possible reaction paths on which C_{60} can be encapsulated into SWNTs.

SWNT samples are made from purified nanotube suspension (tubes@rice, Houston, Texas) [14]. HOPG and SWNT samples were cleaned *in situ* by repeated vacuum annealing to 1200 K under ultrahigh vacuum conditions. C_{60} of 99.5% purity is sublimed from a Knudsen cell at a rate of typically 0.1 monolayers (ML) per minute. Desorption of C_{60} was monitored using the total pressure in the UHV chamber as measured by an ion gauge. Background correction of thermal desorption (TD) traces was carefully cross-checked with TD spectra from species with masses between 4 and 200 a.m.u., the range of our quadrupole mass spectrometer. Absolute coverages and desorption rates were calibrated using the TD spectrum from a saturated and close-packed C_{60} monolayer on HOPG prepared by annealing a few ML thick C_{60} films. Saturation of the HOPG surface with C_{60} could be probed using Xe TD spectra which exhibit distinctly different features if Xe is desorbed from C_{60} or HOPG surfaces. The heating rate was 2.0 K s^{-1}. Additional experimental details can be found elsewhere [15].

The low-coverage TD spectra from the HOPG surface in Fig. 1(a) are typical for zero order desorption kinetics. This is attributed to attractive adsorbate-adsorbate interactions frequently observed for gases physisorbed on graphite. Desorption from the second layer is evident from the additional desorption feature starting on the rising edge of the monolayer feature. The shape and evolution of spectra are consistent with desorption from three-dimensional islands grown by a Volmer-Weber-type mode as reported by a STM study [16]. A careful analysis of TD traces was performed using modified zero order kinetic rate equations where desorption from the nth layer is given by
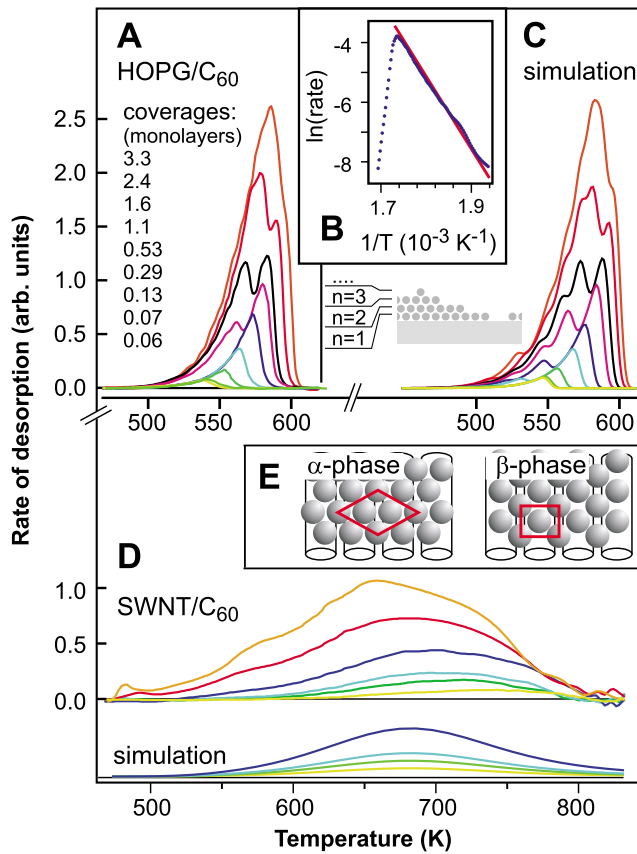
FIG. 1 (color).   Thermal desorption spectra from HOPG and SWNT samples. (a) Series of TD spectra after adsorption of 0.06–3.3 ML of C_{60} on HOPG. (b) Arrhenius plot of the desorption rate at low coverage. (c) Calculated spectra using a multilayer desorption scenario. (d) Spectra from SWNT samples after exposure to similar amounts of C_{60} are broadened and shifted to higher temperatures as are the calculated traces indicating a small increase of the activation energy for desorption from SWNT bundles. (e) Conceivable adsorbate layer arrangements on an idealized SWNT substrate. α and β phases exhibit the largest number of highly coordinated sites within an almost close-packed layer. Unit cells are marked by red lines.

$$\frac{d\Theta_n}{dt} = -\nu_n(1 - \Theta_{n+1})\exp\left(-\frac{E_B}{k_B T}\right). \qquad (1)$$

The factor $(1 - \Theta_{n+1})$ accounts for the constraint of the rate of desorption from the nth layer by the coverage Θ_{n+1} of the $(n + 1)$th layer. The preexponential factor ν for desorption from C_{60} multilayers, $10^{13.2\pm0.3}$ s^{-1}, is obtained from the temperature dependence of the C_{60} vapor pressure [17]. Preexponentials for desorption of VDW bonded monolayers are generally very close to those for desorption from the corresponding solid such that we can use the same factor for desorption from all layers. Our analysis reveals that the activation energy for desorption from the first monolayer is only $(2 \pm 1)\%$ higher than for desorption from the multilayers. This yields an activation energy for C_{60} desorption from the

first layer of 1.69 eV, for which the heat of sublimation E_{sub} from the bulk C_{60} phase of 1.65 eV [17] was used as a reference. Calculated TD traces are shown in Fig. 1(c) where initial coverages needed for the integration of Eq. (1) were estimated from the sequential saturation of individual layers expected for three-dimensional, Volmer-Weber-type growth. Identical results are obtained from the analysis of the rising edge in submonolayer TD spectra shown in Fig. 1(b) as well as from the temperature of the desorption maximum at saturation of the first monolayer.

The activation energies for desorption of VDW bonded adsorbates from graphite commonly include contributions from the binding energy to the surface and the binding energy within two-dimensional adsorbate islands in which the adsorbates are agglomerated. From the common leading edge of the low-coverage TD traces in Fig. 1(a) one can infer that these islands are stable up to at least 580 K, the temperature of desorption. Consequently, the binding energy of a single C_{60} molecule to graphite, 0.85 eV, can be estimated by subtraction of the island binding energy—about $1/12$ the cohesive energy of solid C_{60} for each nearest neighbor, i.e., approximately $6/12\,E_{sub}$.

These values now provide experimental benchmarks guiding the choice of VDW parameters for C_{60}-graphene interactions. To convert the measured binding energy into the appropriate potential parameters, we use the familiar Lennard-Jones potential:

$$V(r) = \frac{C_{12}}{r^{12}} - \frac{C_6}{r^6}. \qquad (2)$$

We then calculate the dependence of different material properties on the C_6 and C_{12} parameters by summation of VDW pair potentials for different structures; see Fig. 2. The binding energy of C_{60} to the graphite surface, including attractive interactions within two-dimensional C_{60} islands, requires that (C_6, C_{12}) parameters are chosen from a point on the long-dashed line. Because of a lack of additional experimental reference data for the C_{60}-graphite system we here chose VDW parameters to match the desorption energy and the graphite lattice constant (dot-dashed line in Fig. 2). The latter should ensure a reasonable description of the repulsive part of the interaction potential. The values used in the following are $C_{12} = 22\,500$ eV Å^{12} and $C_6 = 15.4$ eV Å^6. Within the range of reported values, these parameters also reproduce the graphite c-axis compressibility, the cohesive energy of graphene sheets in graphite, and the VDW contribution to the C_{60} bulk cohesive energy reasonably well. For comparison we have included the parameters used for different graphitic systems by Girifalco *et al.* [13] and for bulk C_{60} interactions by Lu *et al.* [10].

For SWNTs, the curvature of graphene sheets and the resulting asymmetry of π orbitals may induce changes to binding energies on interior and exterior SWNT surfaces. For tube diameters used here we expect such corrections
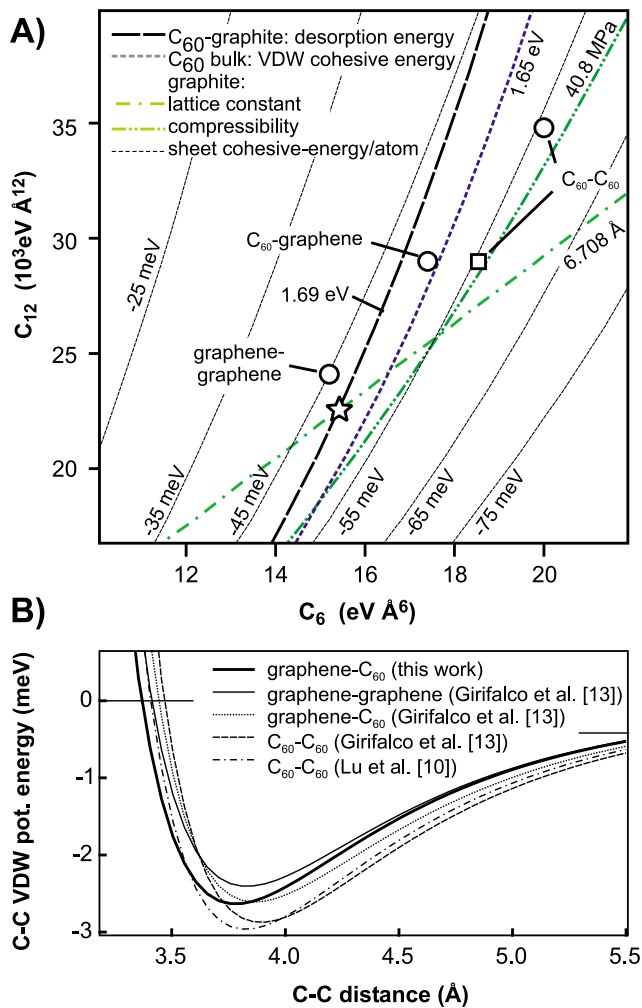
A)

B)

FIG. 2 (color online). (a) van der Waals parameters and the resulting material properties for different systems. (C_6, C_{12} parameters on the long-dashed line, for example, yield the measured activation energy for C_{60} desorption from graphite. To simultaneously account for properties of graphite such as lattice constant or c-axis compressibility we chose a set of (C_6, C_{12}) parameters in the lower part of the graph, marked by a star. The VDW parameters used by Lu *et al.* [10] and Girifalco *et al.* [12,13] are given by open squares and circles, respectively. (b) The corresponding Lennard-Jones potentials.

to scale with the misalignment of π orbitals which—if similar to curvature corrections to the electronic structure—would be of the order of 1%–2% [18]. This does not lead to any significant change of the dynamics or encapsulation probabilities along different reaction paths, and curvature effects are thus neglected in the following discussion.

In the case of thermal C_{60} desorption from SWNT samples, the best agreement of calculated with experimental TD traces is obtained for a desorption energy of 1.7 ± 0.2 eV using a kinetic model introduced elsewhere [15]. The above VDW potential can qualitatively account for this if one assumes that C_{60} is arranged on the SWNT bundle surface in a close-packed manner. Two energeti-

cally favored configurations (α and β phases) in which C_{60} molecules would be mostly adsorbed in highly coordinated sites on the external bundle surface are illustrated in Fig. 1(e). They are determined by the small mismatch of the (9,9) SWNT bundle lattice constant, 15.3 Å with $3/2$ the C_{60} bulk spacing, 15.03 Å and with the C_{60} bulk fcc lattice constant of 14.17 Å. Using the above potential we calculate the C_{60} binding energy in the so-called "groove sites" to be 1.02 eV while it should be about 0.54 eV elsewhere. Including $6/12\, E_{sub}$ and $4/12\, E_{sub}$ for the intralayer binding energies—for six and four nearest neighbors—this would yield C_{60} desorption energies of 1.5 eV and 1.3 eV for the tentatively proposed α and β phases, respectively.

This qualitative agreement with experimental observations encourages us to use the above potentials to discuss the mechanism by which C_{60} is encapsulated in SWNTs. Generally, two distinct mechanisms are conceivable: (a) direct "ballistic" encapsulation of C_{60} from the gas phase through open ends or defects in the tube walls or (b) migration of adsorbed C_{60} from the external tube and bundle surfaces into the SWNT interior [8]. To illustrate the different reaction paths studied here we have reproduced a triple-(10,10) tube arrangement in Fig. 3 which has all the major structural features to be expected in real systems: (1) isolated open ends, (2) nonisolated open ends, and (3) defect openings. As shown in the lower part of Fig. 3 the potential along the reaction path into the individual tube end is found to increase from -0.54 to
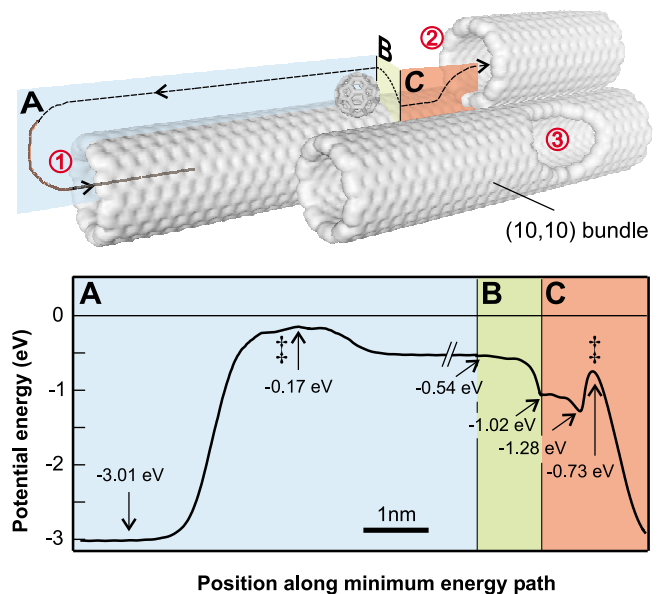

FIG. 3 (color online). Cut through three-dimensional potential energy surface of a small (10,10) tube bundle. Spontaneous encapsulation along all relevant reactions paths is prevented by lip barriers (LBs) due to the lower C_{60} coordination at the rim of SWNTs. Calculations show that encapsulation is most efficient via the head-on approach along the reaction path labeled (c). Transition states are marked by a double dagger (‡).

about -0.17 eV before it drops dramatically to -3.01 eV when C_{60} moves along the outside of the tube over the lip edge into the tube. Similar endohedral binding energies have also been obtained by Girifaclo et al. [12,13]. The large effective barrier for overcoming the lip edge of 0.37 eV is here due to the reduced coordination of C_{60} at the tube end and should prevent C_{60} from spontaneous encapsulation. The origin of this LB is attributed to reduced coordination in analogy to the familiar Ehrlich-Schwoebel barriers near step edges of solid surfaces [19]. Similar barriers are found for all possible surface migration paths into the open tubes.

To identify which reaction path eventually facilitates most efficiently encapsulation we have performed three-dimensional kinetic Monte Carlo trajectory calculations on a rigid bundle similar to the one shown in Fig. 3. Two-dimensional calculations on cuts through the 3D PES would yield misleading results owing to the importance of angular momentum for the encapsulation process. Trajectories were propagated by the velocity Verlet algorithm such that typically 10^5 had energies above the encapsulation threshold for each tested path. The temperature of the statistical ensemble, 650 °C, is close to that of experimental encapsulation runs [6]. Trajectories were defined as successful if their approach from the entrance channel of the PES leads to encapsulation after passing the transition state in less than 100 ps. The probability for encapsulation via the groove at the bottom of a tube opening into the open end, 5×10^{-3}, was found to be highest, while for encapsulation through defect openings or over the isolated LB it was found to be 6×10^{-5} and 3×10^{-5}, respectively. Other conceivable paths were less probable. For comparison with experiments the encapsulation probability needs to be weighted by the attempt frequency resulting from the concentration in a particular entrance channel. Surface concentrations were estimated using the above binding energies and assuming Langmuir kinetics at equilibrium with the C_{60} vapor phase, 650 °C and 10 Pa. For the groove as entrance channel this yields a concentration of 5×10^5 m^{-1} resulting in an attempt frequency of about 2×10^7 s^{-1}. The attempt frequency for entry over the lip of a freestanding tube end is only about 2×10^4 s^{-1} due to the small C_{60} concentration on these low-coordinated, i.e., less strongly binding, sections of the bundle. This eventually leads to a clear preference of the direct "head–on" encapsulation path (c). The rate of successful encapsulation attempts for the defect openings and isolated tube ends are estimated to be 10^3 and 10^5 times smaller, respectively. The rate of ballistic capture from the gas phase through the 2 Å^2 entrance of an open (10,10) tube end would likewise be about 2 orders of magnitude smaller than the head-on capture mechanism.

A direct comparison of the resulting rates with experimental findings is challenging as global filling kinetics are expected to depend on a number of additional factors such as the distribution of tube diameters in the mixed samples and the accessibility of openings. Despite the lack of detailed kinetic data, the results presented here suggest that the calculated filling rates by far exceed what experiments indicate. While some authors have reported filling ratios of up to 70% within less than 2 h at 650 °C [6], others report on an increase in the overall filling ratio over several days [20]. In contrast, the above calculations suggest that tubes could, in principle, be filled within seconds.

In conclusion, we have found that C_{60} encapsulation by SWNTs should proceed most rapidly via migration of *adsorbed* fullerenes and not by ballistic capture from the gas phase despite the significant Ehrlich-Schwobel-like barriers near all types of tube openings. Encapsulation should be most probable for C_{60} adsorbed in grooves by head-on collisions with open tube ends. The high predicted rate of successful encapsulation attempts moreover suggests that the experimentally observed filling rates are not limited by the probability that C_{60} molecules find their way to the entrance of an open tube but rather by the rate at which encapsulated C_{60} molecules or chains of molecules migrate inside the tubes. Interaction with defects on the tube walls or the pressure from residual gas trapped inside of tubes may make it difficult for C_{60} chains to freely migrate and thus slow down the encapsulation process despite the large driving forces expected at the tube entrance.

[1] J. Kong et al., Science **287**, 622 (2000).
[2] S. J. Tans et al., Nature (London) **393**, 49 (1998).
[3] R. Martel et al., Appl. Phys. Lett. **73**, 247 (1998).
[4] B. Vigolo et al., Science **290**, 1331 (2002).
[5] B. W. Smith et al., Nature (London) **396**, 323 (1998).
[6] H. Kataura et al., Synth. Met. **121**, 1195 (2001).
[7] D. J. Hornbaker et al., Science **295**, 828 (2002).
[8] S. Berber et al., Phys. Rev. Lett. **88**, 185502 (2002).
[9] S. Saito and A. Oshiyama, Phys. Rev. Lett. **66**, 2637 (1991).
[10] J. P. Lu et al., Phys. Rev. Lett. **68**, 1551 (1992); X.-P. Li et al., Phys. Rev. B **46**, 4301 (1992).
[11] Ch. Girard et al., Phys. Rev. B **49**, 11425 (1994).
[12] L. A. Girifalco and R. A. Lad, J. Chem. Phys. **25**, 693 (1956).
[13] L. A. Girifalco et al., Phys. Rev. B **62**, 13104 (2000).
[14] A. G. Rinzler et al., Appl. Phys. A **67**, 29 (1998).
[15] H. Ulbricht et al., Chem. Phys. Lett. **363**, 252 (2002).
[16] H. Yu et al., Surf. Sci. **286**, 116 (1993).
[17] J. Abrefah et al., Appl. Phys. Lett. **60**, 1313 (1992).
[18] J. W. Ding et al., Phys. Rev. B **66**, 073401 (2002).
[19] G. Ehrlicha and F. G. Hudda, J. Chem. Phys. **44**, 1039 (1966); R. L. Schwoebel and E. J. Shipsey, J. Appl. Phys. **37**, 3682 (1966).
[20] B. W. Smith et al., J. Appl. Phys. **91**, 9333 (2002).